TU Delft

Delft University of Technology

Document Version
Final published version

Licence
CC BY

Citation (APA)
Plug, N. B., Tan, J., Bosma, S., Carluccio, G., Neto, A., & Llombart, N. (2026). Optimal Current Distributions for Antenna Arrays in Radiative Near-Field Communication Links. *IEEE Open Journal of Antennas and Propagation*, *7*(3), 1062-1077. https://doi.org/10.1109/OJAP.2025.3573016

Important note
To cite this publication, please use the final published version (if applicable).
Please check the document version above.

Copyright
In case the licence states “Dutch Copyright Act (Article 25fa)”, this publication was made available Green Open Access via the TU Delft Institutional Repository pursuant to Dutch Copyright Act (Article 25fa, the Taverne amendment). This provision does not affect copyright ownership.
Unless copyright is transferred by contract or statute, it remains with the copyright holder.

Sharing and reuse
Other than for strictly personal use, it is not permitted to download, forward or distribute the text or part of it, without the consent of the author(s) and/or copyright holder(s), unless the work is under an open content license such as Creative Commons.

Takedown policy
Please contact us and provide details if you believe this document breaches copyrights.
We will remove access to the work immediately and investigate your claim.

This work is downloaded from Delft University of Technology.

Received 14 March 2025; revised 20 April 2025; accepted 18 May 2025. Date of publication 9 June 2025; date of current version 11 June 2026.

Digital Object Identifier 10.1109/OJAP.2025.3573016

Optimal Current Distributions for Antenna Arrays in Radiative Near-Field Communication Links

N. BESCHOOR PLUG [1] (Graduate Student Member, IEEE), J. TAN [1], S. BOSMA [2] (Member, IEEE), G. CARLUCCIO [2] (Senior Member, IEEE), A. NETO [1] (Fellow, IEEE), AND N. LLOMBART [1] (Fellow, IEEE)

[1] Terahertz Sensing Group, Delft University of Technology, 2628 CD Delft, The Netherlands
[2] Advanced Chip Engineering Department, NXP Semiconductors, 5656 AE Eindhoven, The Netherlands

CORRESPONDING AUTHOR: N. BESCHOOR PLUG (e-mail: n.e.beschoorplug@tudelft.nl)

This work was supported by NXP Semiconductors Netherlands B.V. through the Project "Sub-THz Antennas for Next Generation Automotive Radars (STANGAR)."

ABSTRACT We present a design methodology for high-capacity line-of-sight communication arrays in the radiative near-field of each other. We optimize the equivalent aperture current distribution of highly directive antennas in order to obtain noise-limited independent data streams with maximal average signal to noise interference ratio over a range of link distances. The current distributions, equal for the transmit and receive arrays, are found to be defined by the Prolate Spheroidal Wave Function in amplitude and a quadratic phase focusing term. We show that these optimized arrays reach the same coupling levels as when using beamforming techniques without the need for phase control per element. We also demonstrate that this optimization allows the use of fixed beamforming weights rather than highly variable weights over link distance. Finally, we study a 2x2 array at 270 GHz with $6\lambda_0$ diameter elements where the desired aperture current distribution is synthesized using a leaky-wave lens antenna fed by a double-iris slot and a focusing hyperbolic lens. Appropriate modeling of the aperture current distributions results in good agreement between transfer matrix calculations and FW simulations.

INDEX TERMS Leaky-wave lens antenna, line-of-sight, MIMO system, prolate spheroidal wave function, radiative near-field, spatial multiplexing, transfer matrix.

I. INTRODUCTION

IN RECENT literature, there has been an increased interest in the realization of wireless architectures to maximize the spectral capacity between transmit and receive arrays located in the radiative near-field of each other [1], [2], [3]. Requirements on the spectral capacity of these links are expected to even exceed rates of 1 Tbps [2], [3]. To be able to reach these rates one can use large bandwidths which are inherent to higher frequency carriers. One of the most interesting bands in this regard is the recent IEEE standard 802.15.3d [4], which allows up to 70 GHz bandwidth for line-of-sight (LoS) wireless communication systems between 252 GHz and 325 GHz. Designing communication systems at such high frequencies comes with a set of challenges. Two of these challenges are stable power generation and linearity requirements of the amplifiers over the bandwidth [1], [2]. This limits the use of signal processing techniques [5], [6]. These challenges can be overcome by exploiting the spatial multiplexing capabilities of arrays within the radiative near-field [5]. Their transfer matrices in LoS applications are diagonally dominant and inherently full rank, which means that there is very little interference; this makes them ideal for incoherent operation.

In order to maximize power coupling between two antennas in the radiative near-field, several studies have investigated shaping the radiated field of an antenna for wireless power transfer (WPT) applications. A cornerstone paper [7] identified the optimal current distribution for maximum power coupling between two rectangular, linearly polarized apertures to have an amplitude distribution defined by the angular prolate spheroidal wave functions (PSWF) and a quadratic phase focused at the center of the receiver. Recently, [8] and [9] have extended the analysis to circular apertures and found that Bessel and Bessel-Gauss aperture distributions provide high coupling levels, respectively. However, these links for WPT applications are designed to

© 2025 The Authors. This work is licensed under a Creative Commons Attribution 4.0 License.
For more information, see https://creativecommons.org/licenses/by/4.0/

have maximum coupling at a specific link distance within the radiative near-field (RNF) between two LoS antennas. Therefore, they are not optimized to minimize interference from other antennas within an array, which is required for incoherent communication arrays.

Shaping the radiated field of a single antenna has also been studied in the context of high-capacity communication applications where the coupling must remain high over a range of link distances [10], [11]. To increase the spectral capacity of the link, the antenna in [10] is designed in such a way that the first three OAM (orbital angular momentum) modes are supported. Beamforming techniques are also applied in [11] to an array of slots to create four orthogonal modes with the element excitation differing only in phase by 180°. These studies show that beamforming is a highly effective technique to increase the spectral capacity within the RNF. In the far-field of the antennas, only the uniform mode contributes to the spectral capacity [11]. However, lossy feeding networks at high frequencies are required in these previous works. In [6], the spectral capacity of arrays for communication systems is increased by exploiting spatial multiplexing. Here, highly directive antenna beams are tilted by a linear phase towards the receiver, reducing the interference. This solution gives an extremely high spectral capacity at a specific link distance in the radiative near-field. The spectral capacity of the design in [6] however, is limited by the interference from the other antennas within the transmit array without the use of beamforming. In theory, it is also possible to use incoherent arrays over a link distance range by exploiting spatial multiplexing through directive antennas only.

In this study, we extend the work of [6] by optimizing the equivalent aperture currents with the aim of maximizing the overall link spectral capacity in a region referred to as the incoherent region (half the far-field distance). This array solution is scalable in the number of elements and element size depending on requirements and constraints such as link distance, maximum dimensions, total transmit power, and system noise figure. The scope of this paper is to provide design guidelines for incoherent antenna arrays and to address the challenges communication systems face at high frequencies and large bandwidths. These designs could be realized with integrated technologies with low power output requirements and moderate system noise performance. Moreover, designing the arrays, as proposed here, enables the use of beamforming weights to further increase the spectral capacity that are stable in the entire incoherent region, contrary to standard LoS multiple-input multiple-output (MIMO) architectures [12].

The article is structured as follows. In Section II we elaborate on the problem under investigation and introduce a method of evaluating the coupling between the antenna elements. We derive the optimization strategy of the spectral capacity of a LoS array from this. In Section III we study the performance of the aperture current distribution given in [7] and apply it to circular apertures. In Section IV, the aperture current distribution is optimized for a relevant case with different levels of system noise figure. The results are compared to an optimized Gaussian distribution. In Section V a method of evaluating the coupling between beamforming distributions is derived from the method of evaluation of the coupling between antenna elements. Using this method, the performance of the incoherent array is compared to its performance when using beamforming techniques. Finally, in Section VI, a lens antenna array is designed that has an equivalent aperture current distribution that matches the optimized current distribution. Full-wave CST simulations of this array are used to validate the transfer matrix model.

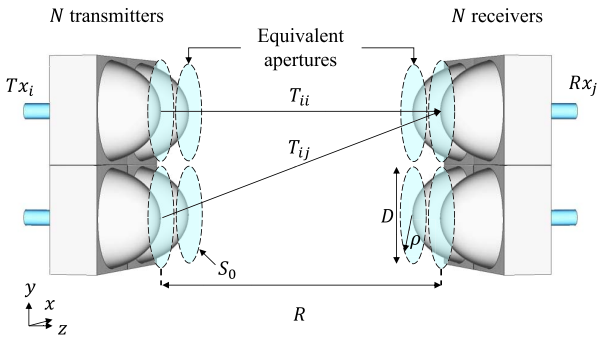


FIGURE 1. LoS communication scenario where the Tx and Rx array face each other. The lens array elements are modeled by their equivalent aperture current distribution defined over a circle S_0 with the diameter of the lens located on top of the lenses.

II. PROBLEM DEFINITION

Consider the LoS communication scenario depicted in Fig. 1, where transmit (Tx) and receive (Rx) lens antenna arrays, each with N elements, face each other at link distance R and are perfectly aligned. Each lens has a diameter D. Our objective is to maximize the spectral capacity of N simultaneous LoS communication links. We can achieve this spatial multiplexing using directive, focusing antennas without the need for signal processing-based MIMO architectures [6] as long as the link distance is not too large. Specifically, the individual Tx and Rx lens elements facing each other must be in the radiative near-field of each other. In this paper, the RNF region is defined as the region between the considered antenna and half the far-field distance R_{ff} of a single lens element, i.e., $0 < R \leq R_{ff}/2 = D^2/\lambda$. The fields radiated by each element can then be considered collimated and, therefore, the interference at the non-LoS receivers will be much lower than for a far-field link distance.

A. SPECTRAL CAPACITY FROM SCATTERING PARAMETERS

The spectral capacity of incoherent LoS arrays using a relatively narrow bandwidth is approximately the sum of the N individual channels, $j = 1, \ldots, N$:

$$C = \sum_{j=1}^{N} \log_2\left(1 + \frac{S_{Rx_j}}{I_{Rx_j} + N_{Rx_j}}\right) \quad \left[\frac{\text{bit}}{\text{s} \cdot \text{Hz}}\right], \tag{1}$$

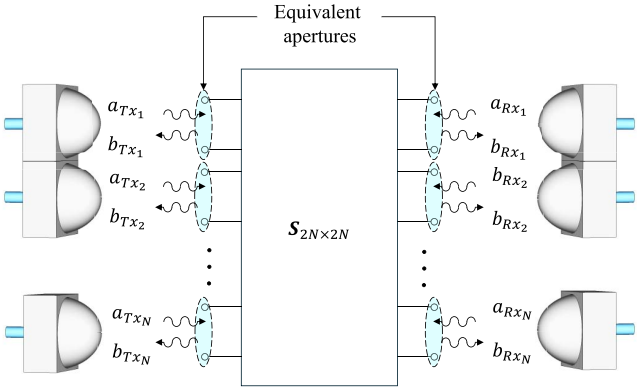


FIGURE 2. 2*N*-port network representation of the LoS communication scenario given in Fig. 1. The reference planes for the S-matrix describing this network are defined at the locations of the equivalent apertures.

where j represents a single receiver. The quotient in the argument of the logarithm is the signal-to-noise-plus-interference ration (SNIR) where S_{Rx_j} is the received signal spectral power at Rx_j, I_{Rx_j} the interference spectral power received by Rx_j, and N_{Rx_j} is the average noise spectral power at Rx_j. The N_{Rx_j} is assumed to be identical per receiver and is defined as:

$$N_{Rx_j} = k_B T(N_F + 1) \quad \left[\frac{\mathrm{W}}{\mathrm{Hz}}\right], \tag{2}$$

where k_B is Boltzmann's constant, T is the temperature (assumed 290 K here), and N_F is the system noise figure. Equation (1) is a modification of the classical spectral capacity equation of Shannon [13] by including the effect of the interference in the array. It gives a theoretical upper limit of the achievable spectral capacity level including interference, where all the interference contributions are added incoherently.

To calculate the power level and the interference level received at Rx_j in (1) the transfer matrix of the system must be calculated. This can be done using circuit theory as is described in literature [14], [15]. The lens antennas in Fig. 1 are modeled through equivalent current distributions located on top of the lenses, depicted by the apertures S_0. The system of these $N \times N$ apertures is modeled as a $2N$-port network, which is shown in Fig. 2, where the incident (a) and reflected (b) signal waves are defined from the antenna equivalent apertures and are related by the scattering parameter matrix of size $2N \times 2N$: $\boldsymbol{b} = \boldsymbol{S}\boldsymbol{a}$. These terms can be expanded so that they are written in terms of the transmitter and receiver as:

$$\begin{bmatrix}\boldsymbol{b}_{Tx}\\ \boldsymbol{b}_{Rx}\end{bmatrix} = \begin{bmatrix}\boldsymbol{S}_{TxTx} & \boldsymbol{S}_{TxRx}\\ \boldsymbol{S}_{RxTx} & \boldsymbol{S}_{RxRx}\end{bmatrix}\begin{bmatrix}\boldsymbol{a}_{Tx}\\ \boldsymbol{a}_{Rx}\end{bmatrix}, \tag{3}$$

where the bold terms represent vectors or matrices. The submatrices in the S-parameters have dimension $N \times N$ and the reflected and incident waves of both the Tx and Rx arrays are defined as $N \times 1$ vectors:

$$\boldsymbol{a}_{Tx,Rx} = \begin{bmatrix}a^{i,j=1}\\ a^{i,j=2}\\ \vdots\\ a^{i,j=N}\end{bmatrix}; \quad \boldsymbol{b}_{Tx,Rx} = \begin{bmatrix}b^{i,j=1}\\ b^{i,j=2}\\ \vdots\\ b^{i,j=N}\end{bmatrix}. \tag{4}$$

Assuming that the receivers are terminated by a certain loading condition, the incident and reflected waves on each Rx_j are related by a reflection coefficient. The set of equations from (3) can be written as:

$$\boldsymbol{b}_{Tx} = \boldsymbol{S}_{TxTx}\boldsymbol{a}_{Tx} + \boldsymbol{S}_{TxRx}\boldsymbol{\Gamma}_L\boldsymbol{b}_{Rx}, \tag{5}$$

$$\boldsymbol{b}_{Rx} = \boldsymbol{S}_{RxTx}\boldsymbol{a}_{Tx} + \boldsymbol{S}_{RxRx}\boldsymbol{\Gamma}_L\boldsymbol{b}_{Rx}. \tag{6}$$

where $\boldsymbol{\Gamma}_L$ is the reflection coefficient which is a diagonal $N \times N$ matrix. Solving (6) for $\boldsymbol{b}_{Rx}$ gives:

$$\boldsymbol{b}_{Rx} = (\boldsymbol{I} - \boldsymbol{S}_{RxRx}\boldsymbol{\Gamma}_L)^{-1}\boldsymbol{S}_{RxTx}\boldsymbol{a}_{Tx} \overset{\text{def}}{=} \boldsymbol{T}\boldsymbol{a}_{Tx}, \tag{7}$$

where $\boldsymbol{I}$ is the $N \times N$ identity matrix. Matrix $\boldsymbol{T}$ is the transfer matrix in which every row represents the signal transfer to one receiver. If we further assume that the mutual coupling within the elements of the arrays is negligible ($\boldsymbol{S}_{TxTx} = 0$ and $\boldsymbol{S}_{RxRx} = 0$), an assumption valid for arrays with electrically large spacing, (7) is simplified to:

$$\boldsymbol{T} = \boldsymbol{S}_{RxTx}. \tag{8}$$

In this paper, the transfer matrix $\boldsymbol{T}$ is calculated using the coupling integral between the radiated field from the equivalent Tx and Rx array element current distributions as described in Appendix A [6] and summarized here:

$$T_{ij} = \frac{V_{oc}^i I_0^j}{\sqrt{16 P_{rad}^i P_{rad}^j}}, \tag{9}$$

where $P_{rad}^{i,j}$ represents the radiated power from both apertures and where the numerator is a reaction integral between the electric and magnetic fields radiated by the current distributions defined over the equivalent aperture of Tx_i and the electric and magnetic current distributions defined over the equivalent aperture of Rx_j, evaluated over the surface of Rx_j, S_0, as:

$$V_{oc}^i I_0^j = \iint_{S_0}\left[\vec{h}_i(\vec{r})\cdot\vec{m}_j(\vec{\rho}) - \vec{e}_i(\vec{r})\cdot\vec{j}_j(\vec{\rho})\right]dA. \tag{10}$$

We assume that $[\vec{m}_{i,j}(\vec{\rho}), \vec{j}_{i,j}(\vec{\rho})]$ are defined as Huygens' sources propagating in $+\hat{z}$ for the transmitters and $-\hat{z}$ for the receivers. The electric and magnetic current densities are defined as:

$$\vec{j}_{i,j}(\vec{\rho}) = -\frac{I_0}{D} g_{i,j}(\rho)\mathrm{domain}(\vec{\rho}, S_0)\hat{y}, \tag{11}$$

$$\vec{m}_{i,j}(\vec{\rho}) = \pm\frac{\zeta_0 I_0}{D} g_{i,j}(\rho)\mathrm{domain}(\vec{\rho}, S_0)\hat{x}, \tag{12}$$

where I_0 is the current feeding the antenna, D is the linear dimension of the antenna aperture, and $g(\rho)$ represents

a complex-valued distributions whose maximum value is normalized to one in the considered domain S_0, see Fig. 1, and domain$(\vec{\rho}, S_0)$ is a function which defines the aperture and is equal to 1 for $\vec{\rho} \in S_0$. The diagonal entries of matrix $\boldsymbol{T}$, T_{ii}, therefore represent the coupling between two LoS apertures and the off-diagonal terms, T_{ij}, the coupling between non-LoS elements. Once $\boldsymbol{T}$ (8) is known, we can evaluate S_{Rx_j} and I_{Rx_j} needed for the spectral capacity (1).

In this work, we want to study configurations where each transmitter and receiver can operate independently and therefore, no beamforming techniques are applied. For that reason, the received power corresponds to the LoS link $(j = i)$ and is calculated as:

$$S_{Rx_j} = P_{Tx_i}|T_{ii}|^2, \tag{13}$$

where P_{Tx_i} is the input power of Tx_i. For a specific choice of I_0 this will be equal to P^i_{rad} (Appendix A, (37)). The interference is the sum of the power received by Rx_j from all other transmitters $i \neq j$ and is calculated as:

$$I_{Rx_j} = \sum_{i \neq j} P_{Tx_i}|T_{ij}|^2. \tag{14}$$

B. OPTIMIZATION OF SPECTRAL CAPACITY

We optimize the spectral capacity (1) by maximizing the SNIR over the link distance in which this system operates. This approach will find the optimal relation between high LoS coupling and low interference for specific transmit power P_{Tx_i} and system noise N_{Rx_j}. To do so, we seek to minimize the average reciprocal of the SNIR over range for a single receiver Rx_j:

$$\min\left\{\frac{1}{\overline{\text{SNIR}_j}}\right\} = \min\left\{\frac{1}{R_l}\sum_{l=1}^{R_l}\left(\frac{N_{Rx_j} + I^l_{Rx_j}}{S^l_{Rx_j}}\right)\right\}, \tag{15}$$

where R_l is the number of points in the desired range and the index l represents each point in range. To minimize (15), the parameters that define the equivalent aperture current distribution are variable, as changes in the amplitude and phase of this current distribution will lead to different transfer coefficients in (13) and (14).

III. OPTIMAL CURRENT DISTRIBUTION FOR POWER COUPLING FOR SISO LINKS IN THE FRESNEL REGION

Previous studies have explored optimal equivalent aperture current distributions that maximize power transfer between two antennas located in the Fresnel region [7], [8], [9], [16], [17]. These current distributions maximize the reaction integral in (10). When two identical apertures are within the Fresnel region of each other [18], (10) can be simplified as described in [7] to the following expression:

$$V_{oc}I_0 = \frac{jk_0\zeta_0 e^{-jk_0F}}{\pi F}\iint_{S_0} g_j(\rho)e^{-j\frac{k_0\rho^2}{2F}} \iint_{S_0} g_i(\rho')e^{-j\frac{k_0\rho'^2}{2F}}e^{j\frac{k_0}{F}\vec{\rho}\cdot\vec{\rho}'}dS_0'dS_0, \tag{16}$$

where k_0 is the wavenumber in free-space, ζ_0 is the free-space impedance, F is the focal distance of the quadratic phase term which is equal to the link distance, and the prime indicates the aperture of the transmitter (shown schematically in Appendix A, Fig. 16). In this section the optimal current distribution for a rectangular aperture in the Fresnel region, derived in [7], is revised and the application of this optimal current distribution is extended to circular apertures.

A. OPTIMAL CURRENT DISTRIBUTION FOR SQUARE APERTURES

Applying the Fresnel approximations to the integral equation for the coupling between two apertures in the RNF leads to (16). Due to the approximation on the phase there is a quadratic phase term $e^{-j(k_0(x^2+y^2)/2F)}$ which is multiplied with the complex-valued function $g_{i,j}(x, y)$ from which the currents are defined (11) and (12). To maximize the coupling between the apertures $g_{i,j}(x, y)$ must contain the complex conjugate to this quadratic phase term. The remaining current distribution, $f(x, y)$, should also be conjugate matched between transmitter and receiver for maximum coupling. Therefore, the transmit and receive equivalent aperture currents can be written as:

$$g_i(x', y') = f(x', y')e^{j\frac{k_0x'^2}{2F}}e^{j\frac{k_0y'^2}{2F}}, \tag{17}$$

$$g_j(x, y) = f(x, y)^*e^{j\frac{k_0x^2}{2F}}e^{j\frac{k_0y^2}{2F}}. \tag{18}$$

To find the optimal distribution, (16) is treated as an eigenfunction problem in [7], where the eigenfunctions represent the current distributions $f(x, y)$ and the corresponding eigenvalues represent the power transfer. For rectangular apertures, this can be solved analytically and the eigenfunctions are the Prolate Spheroidal Wave Function (PSWF) of the zeroth order, S_{00}:

$$f(x, y) = S_{00}\left(c, \frac{x}{D/2}\right)S_{00}\left(c, \frac{y}{D/2}\right), \tag{19}$$

where x and y span the equivalent aperture defined Fig. 1, and c is defined as [7]:

$$c = \frac{k_0(D/2)^2}{F}. \tag{20}$$

This parameter can be related to the Fresnel number $F_\# = D^2/F\lambda_0$ of a Gaussian beam through:

$$c = \frac{\pi}{2}F_\#. \tag{21}$$

The PSWF introduces a taper in the amplitude which increases with c, and therefore with smaller F. The LoS coupling (16) between two square apertures with the optimal current distribution defined in (17) and (18) give the same result as [7]. This and the corresponding edge taper are plotted in Fig. 3. The coupling is almost unity as the apertures are well within the Frensel region of each other (large c) and decreases as the apertures move into the far-field of each other. However, due to the Fresnel approximations which lead to (16) this can only be applied to

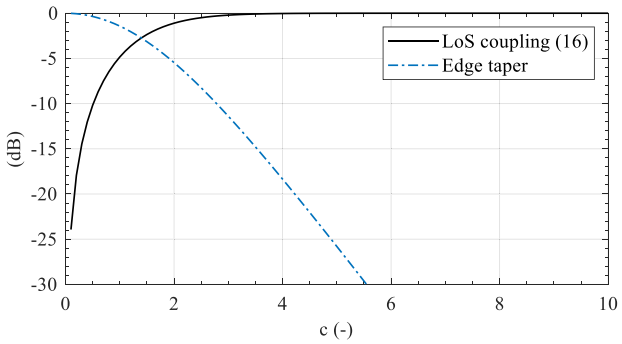


FIGURE 3. LoS coupling (16) in the black solid line, corresponding to the values of T_{opt} in Table I from [7], and the required edge taper between two apertures in the blue dotted-dashed line versus c.

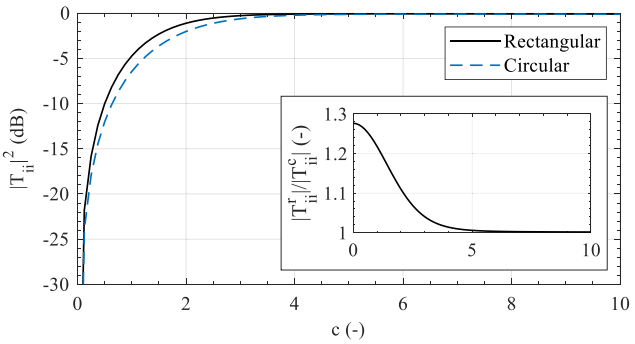


FIGURE 4. Coupling between square (black) and circular (blue) apertures with PSWF current distribution and a quadratic phase term. The inset shows the ratio between the two.

electrically large apertures. For electrically small apertures, the full expression of the radiative Green's function (RGF) must be used to calculate the coupling. The properties of the PSWF are discussed in Appendix B.

B. APPLICATION TO CIRCULAR APERTURES

Optimal power coupling between two square apertures with linearly polarized fields has been studied extensively in the literature numerically [16], [17]. The cases studied all have tapered amplitude or Gaussian distributions. Instead in [19], an analytical solution based on Generalized Prolate Spheroidal Functions is provided. In this section, we study the coupling between two circular apertures using the PSWF of the zeroth order as amplitude distribution. This current distribution is rotationally symmetric and therefore (19) can be written as:

$$f(\rho) = S_{00}(c, \rho). \tag{22}$$

In Fig. 4 the coupling between two circular apertures of diameter D with the current distribution defined in (22) is compared to the coupling between two square apertures with sides of dimension D with the current distribution defined in (19). It is apparent that large values of c give the same level of coupling, indicating that a circular aperture (with smaller area) is equally effective as a square aperture (of the same dimension) in the RNF. For small values of c (reaching the far-field), the coupling is indeed different. The ratio of the coupling between two square apertures to the coupling between two circular apertures is plotted in the inset of Fig. 4. This shows that in the far-field the coupling between the square apertures is a factor $4/\pi$ times larger, which is the ratio of the apertures' area. In the near-field however, the coupling is the same – this justifies the extension of the optimal current distribution of [7] to circular apertures in the Fresnel region. Although (22) is not proven optimal, it is suitable as a starting point for further numerical optimization.

IV. OPTIMIZING SNIR PERFORMANCE OF ARRAYS WITH FIXED APERTURE CURRENT DISTRIBUTIONS

The optimal current distribution has been previously studied for the single-input single-output (SISO) case for a single link distance [7] but has not been extended to an incoherent array for a range of link distances before. To do so, interference must be considered. In this case, the optimal current distribution is one which simultaneously maximizes the LoS coupling (13) and minimizes the received interference (14). A single metric which captures these terms is the SNIR. In the previous section, we observed that the ideal equivalent aperture distribution for a SISO link, (17), (18) and (19), changes for every value of c. For a realistic design, it is necessary to fix the value of c for a varying link distance and varying frequency within the bandwidth. However, in a practical system, c will be limited by the required edge taper (Fig. 3), aperture dimensions, and targeted link distances in terms of wavelength. The fixed current distribution will impact the SNIR over the range of link distances.

To find a single, optimal current distribution we will use (15). As a relevant case, we assume that each array has $N = 4$ elements (see Fig. 1) with a diameter of $D = 6\lambda_0$, at $f_0 = 270$ GHz. The arrays must be able to work incoherently until a link distance of $R_{ff}/2$, in this case from $5\lambda_0$ to $35\lambda_0$. We assume a total spectral input power P_{tot} of -10 dBm is available and is divided equally over the array elements: $P_{Tx_i} = P_{tot}/N$. We also assume a system noise figure of $N_F = 15$ dB. Furthermore, we assume that the arrays are perfectly aligned. For the current scenario, $P_{Tx_i} = -16$ dBm and $N_{Rx_j} = -50$ dBm (from (2)), leading to a maximum theoretical signal-to-noise ratio (SNR) of 34.5 dB.

Under these assumptions, we have calculated the received LoS signal (13) and interference (14) in a single receiver. These are shown in Fig. 5 together with the spectral noise power. Based on these levels it is possible to impose an upper and lower limit on c and to use it as a range for the optimizer (15). The lower limit of $c = \pi/2$, indicated with the left vertical dashed line, corresponds to half the far-field distance of a single aperture ($F = D^2/\lambda_0$). For c lower than this point, the interference approaches the LoS coupling. A practical upper limit of $c < 4.2$, indicated with the right vertical dashed line, can be defined by imposing a maximal signal-to-interference ratio (SIR) of 40 dB. Beyond this point, i) accuracy limits of the transfer matrix-based

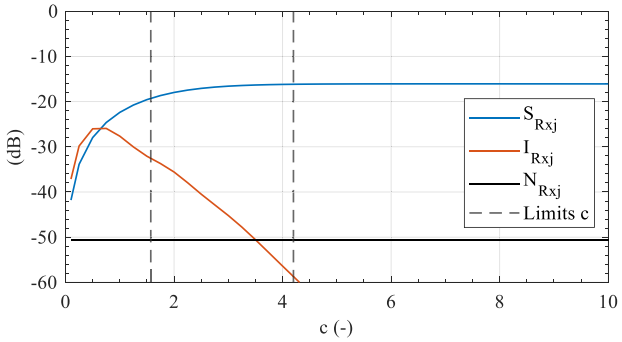


FIGURE 5. Signal and interference levels in 2 × 2 array with total spectral input power of −10 dBm and the average spectral noise power of −50 dBm. When $I_{Rx_j} < N_{Rx_j}$ we define tthe system to be noise-limited.

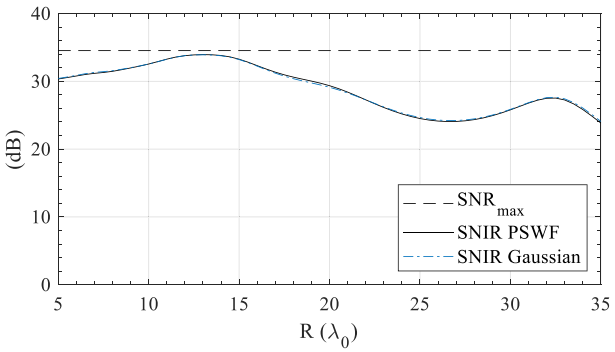


FIGURE 6. Maximum theoretical SNR = P_{Tx_j}/N_{Rx_j} of 34 dB and SNIR using PSWF ($c = 3$, $F_p = 11.4\lambda_0$) and Gaussian ($w_0 = 2.7\lambda_0$, $F_p = 11.6\lambda_0$) amplitude distributions over the considered range.

calculations based on field coupling are reached since the field levels at the non-LoS apertures are extremely low, and ii) the required edge taper of the current distribution is more than 25 dB (see Fig. 3), which is difficult to realize with lens antennas.

A. OPTIMAL EQUIVALENT CURRENT DISTRIBUTION USING PSWF

We then proceed to minimize the SNIR (15). To do this, we, differently from the optimal function for SISO links in [7], decouple the focal distance of the quadratic phase from the amplitude distribution. The focal term is now F_p and the term controlling the amplitude distribution F_a. The optimal current distribution is therefore written as:

$$g_{i,j}(\rho) = S_{00}(c, \rho) e^{j\frac{k_0\rho^2}{2F_p}}, \tag{23}$$

with,

$$c = \frac{k(D/2)^2}{F_a}. \tag{24}$$

We have found an optimal solution of $c = 3$ (corresponding to an edge taper of -11.4 dB) and $F_p = 11.4\lambda_0$ which is within the limits of c defined earlier. The SNIR of the system over the RNF is plotted in Fig. 6. For $R < 15\lambda_0$ the SNIR is very high and even approaches the maximum theoretical SNR. In this range, the system is noise limited. The peak of the SNIR corresponds to maximum LoS coupling due to a conjugate match between the radiated field and the equivalent currents of the corresponding receiver. For $R > 15\lambda_0$ a lower SNIR is obtained due to an increase in interference caused by the spreading of the radiated field. Over half the far-field distance, the SIR remains above 25 dB, enabling four independent communication channels.

B. EFFECT OF DIFFERENT NOISE LEVELS ON OPTIMIZER SOLUTION

Next, we study the effect of system noise on the solution of the optimizer. The maximum theoretical SNR and corresponding optimized solution are shown in Table 1 for different noise figures N_F. The corresponding SNIR as a function of link distance is shown in Fig. 7. For large values of N_F the system is clearly noise limited as the SNIR curve is nearly flat. Under these conditions, a lower taper (lower c) is optimal because it will increase the LoS coupling while maintaining an interference below the spectral noise power. For lower N_F, the level of the interference starts to play a more dominant role, and current distribution must have a higher taper. Below roughly $N_F = 15$ dB, the received spectral noise power is so low that it no longer plays an important role and the optimizer solution settles at $c \approx 3$, $F_p \approx 11.3\lambda_0$. This can be seen in Fig. 7, where the SNIR no longer has a flat response (N_0 (2) is assumed constant over R) and instead follows the fluctuating behavior of the interference (14). For large values of R the SNIR curves no longer approach the value of theoretical maximal SNR. In these cases, the small changes in the optimizer solution only have an effect over very small ranges. This is also why the focal distance decreases.

TABLE 1. Optimizer solution for optimal equivalent current distribution using PSWF for different system noise levels N_{Rx_j}.

N_F	SNR_{max}	c	F_p
35 dB	14.5 dB	2.75	$20.58\lambda_0$
25 dB	24.5 dB	3.04	$12.49\lambda_0$
15 dB	34.5 dB	3.03	$11.39\lambda_0$
5 dB	44.5 dB	3.02	$11.28\lambda_0$

C. OPTIMIZATION OF GAUSSIAN AMPLITUDE DISTRIBUTION

In the literature, as mentioned in Section III, there are works that suggest the near-optimal current distributions for circular apertures are based on Gaussian amplitude distributions [17]:

$$f(\rho) = e^{-\frac{\rho^2}{w_0^2}}, \tag{25}$$

where w_0 defines the Gaussian waist. Therefore, as a final step, we want to compare the obtained results using PSWF amplitude current (22) to those using (25). The same

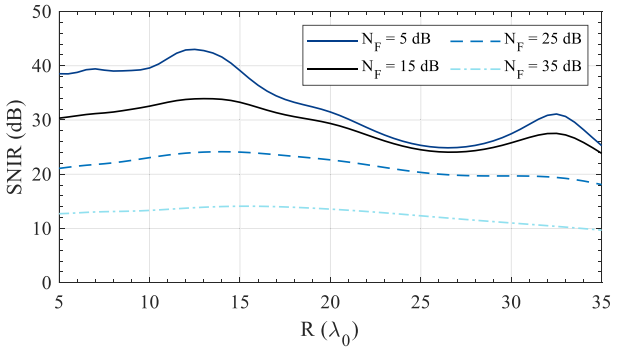


FIGURE 7. Effect of system noise level on the optimized SNIR over the entire range. An N_F of 15 dB is assumed for the design of the system.

optimization procedure is applied, with the transmit and receive equivalent current distributions written as:

$$g_{i,j}(\rho) = e^{-\frac{\rho^2}{w_0^2}} e^{j\frac{k_0\rho^2}{2F_p}}, \tag{26}$$

where the parameters to optimize are the Gaussian waist w_0 and the focal distance F_p. The optimized solution for a Gaussian distribution under the assumptions described in Section IV is $w_0 = 2.7\lambda_0$ (corresponding to an edge taper of -10.7 dB) and $F_p = 11.6\lambda_0$. The corresponding SNIR is plotted in blue in Fig. 6 and is almost identical to the SNIR obtained with the PSWF. This suggests that we can approximate the PSWF distribution with a Gaussian distribution which is typically used in quasi-optical systems.

V. IMPROVEMENT OF CAPACITY USING BEAMFORMING TECHNIQUES

To understand how much further the SNIR can be improved, we can evaluate the system transfer matrix assuming the possibility of employing beamforming techniques, even if it comes at the cost of added system complexity. The goal is to understand whether we can use a fixed set of beamforming distributions that can operate over the entire range and frequency band. For this, we need to modify the evaluation of the transfer matrix.

A. DERIVATION OF COUPLING BETWEEN BEAMFORMING CURRENT DISTRIBUTIONS

The beamforming transfer matrix $\boldsymbol{B}$, with entries B_{mn}, represents the coupling between the beamforming distribution m of the transmit array and beamforming distribution n of the receive array. Therefore, similar to the transfer matrix $\boldsymbol{T}$ with entries T_{ij} (9), the entries on the diagonal ($m = n$) of $\boldsymbol{B}$ represent the coupling between identical beamforming distributions and the other entries ($m \neq n$) represent the interference between the different beamforming distributions. For an array with M elements, there are M possible orthogonal distributions [11]. Since we operate the array, with optimized equivalent aperture current distributions, in the incoherent region, the radiated fields of the Tx apertures remain collimated and the interference level at the Rx apertures is negligible. We can then assume that the LoS radiated field on the corresponding Rx aperture resembles current distribution on the corresponding Rx aperture. Therefore, the optimal beamforming weights for the Rx apertures maximizing the coupling are the complex conjugate, denoted by the asterisk, of the weights of the Tx apertures:

$$\mathbf{W}_{Tx} = \mathbf{W}_{Rx}^{*} = \begin{bmatrix} w_{11} & w_{12} & w_{13} & w_{14} \\ w_{21} & w_{22} & w_{23} & w_{24} \\ w_{31} & w_{32} & w_{33} & w_{34} \\ w_{41} & w_{42} & w_{43} & w_{44}, \end{bmatrix} \tag{27}$$

where each row of $\mathbf{W}_{Tx}$ and $\mathbf{W}_{Rx}$ contains the weights whose linear combination allows the excitation of a specific beamforming distribution, and where each column assigns these weights to the corresponding array element. In standard MIMO optimization techniques, the Tx and Rx weights can be different and are found via a Singular Value Decomposition (SVD) technique [20].

Appendix C describes the steps to evaluate the transfer matrix $\boldsymbol{B}$ associated with the beamforming distributions. This matrix can be calculated by multiplying the individual aperture couplings of $\boldsymbol{T}$ by the corresponding weights of distributions m and n described in (27) as follows:

$$b_{mn} = \frac{\mathbf{W}_{Rx}\mathbf{T}\mathbf{W}_{Tx}^{T}}{\sqrt{\sum_{j=1}^{M}|w_{n,j}^{*}|^2 \sum_{i=1}^{M}|w_{m,i}|^2}}. \tag{28}$$

It is possible to evaluate the spectral capacity similar to (1) by using $\boldsymbol{B}$ instead of $\boldsymbol{T}$. In this case the received spectral power of the link, corresponding to the same beamforming distribution ($n = m$), is calculated in a way that is similar to (13), as:

$$S_{Rx_n} = P_{Tx_m}|B_{mm}|^2, \tag{29}$$

where P_{Tx_m} is the spectral input power for mode m of the array. The interference received from all other transmitted distributions into the n-receiver distribution can be evaluated, similar to (14), as the sum of the receiver spectral power from all other transmitted distributions $m \neq n$ as:

$$I_{Rx_n} = \sum_{n\neq m} P_{Tx_m}|B_{mn}|^2. \tag{30}$$

If the beamforming distributions are orthogonal to each other the interference will be zero. Using this general formulation, we can estimate the impact of the interference between distributions on the spectral capacity when the modes are not orthogonal.

B. COMPARISON OF PERFORMANCE OF INCOHERENT ARRAYS AND ARRAYS WITH BEAMFORMING WITH OPTIMIZED EQUIVALENT CURRENT DISTRIBUTIONS

MIMO theory [20] can be applied to find the ideal unconstrained beamforming weights that will maximize the spectral capacity for every link distance by imposing orthogonality between the distributions. However, it would

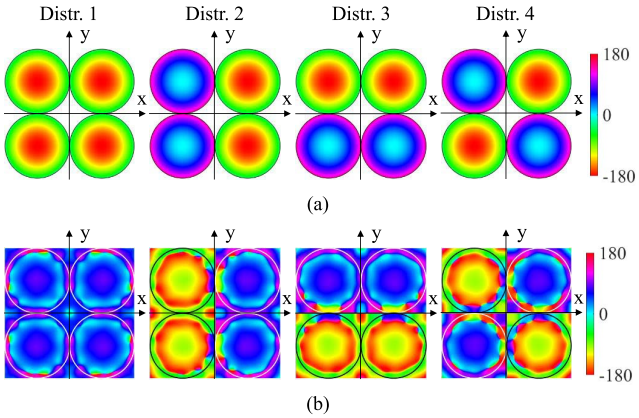


FIGURE 8. In (a) the phase of the fixed weights for the four beamforming distributions over the Rx array (W_{Rx}) are shown. In (b) the phase of radiated field from the Tx array with the fixed beamforming distributions ($W_{Tx} = W^*_{Rx}$) are shown at $R = 10\lambda_0$. Due to the definition of the weights in (27) the radiated Tx fields and Rx currents are each other's conjugate.

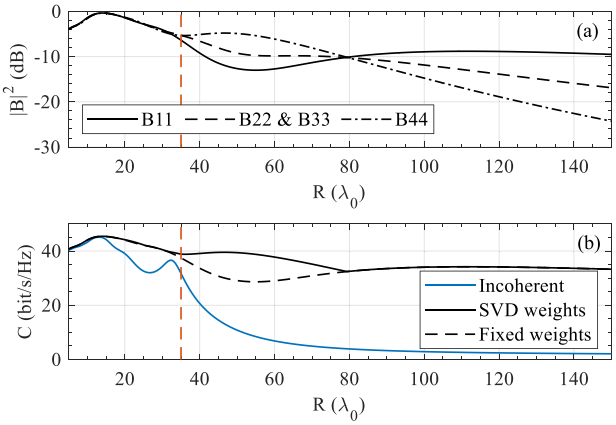


FIGURE 9. In (a) the LoS coupling between the fixed modes (B_{ii}) and in (b) the spectral capacity for the incoherent and coherent (beamforming implemented through SVD or fixed weights) array for current scenario.

be convenient in terms of system implementation to realize this with simple beamforming weights that are not dependent on distance. For a 2×2 array, four orthogonal distributions using only 180° phase differences were proposed in [11]. We apply these same weights, from here on referred to as fixed weights, to the optimized incoherent array discussed in Section IV-A. In Fig. 8b the phase of these four distributions over the Rx array is shown. Fig. 8a shows the radiated field of the Tx array over the Rx array which is the complex conjugate of the Rx currents.

The LoS coupling for these beamforming distributions is compared to the LoS coupling of the single element optimized current distribution in Fig. 9a. The S_{Rx_n} is approximately the same as that of the LoS single element coupling with the optimized currents over the incoherent range (indicated by the red dashed vertical line), whereas the cross-coupling between the beamforming distributions is negligible (< -50 dB).[1] As a result, the spectral capacity in Fig. 9b increases significantly. In the incoherent region the spectral capacity remains above 36 bit/s/Hz. Within the incoherent region, the beamforming weights improve the spectral capacity in the region where the SNIR of the incoherent array is interference-limited, see Fig. 7. This is because the beamforming weights remove the interference in the radiative near-field. As the distributions utilize the entire array area, the operational range is increased by a factor n^2. Within the operational region ($R < n^2 R_{ff}$) all four distributions can be used, after this, only the main distribution remains [11].

In this section, we showed that stable beamforming weights can be used to improve the spectral capacity of the array with optimized equivalent aperture current distributions over the entire incoherent region. This is due to the low interference level at every Rx receiver in the incoherent array after the optimization. This enables us to define the Rx currents as the conjugate of the Tx ones. Beyond the incoherent region, the interference will start to play a dominant role in the uniformity of the coupling between identical beamforming distributions and their respective optimal weights. Therefore, to be able to apply fixed beamforming weights to improve the spectral capacity, the mutual coupling within the Tx and Rx arrays needs to be lower than the incoherent interference between the antennas in Tx and Rx. In the case of this scenario, that would mean that it is equal to -30 dB. We also showed that the spectral capacity is the same in the region where the equivalent currents are optimized when using the fixed weights as when the weights generated through the SVD (optimal for every link distance). This can be seen from the solid line in Fig. 9b.

C. PERFORMANCE COMPARISON WITH MIMO ARRAYS WITHOUT CURRENT OPTIMIZATION

For comparison, we consider a standard LoS MIMO array architecture [21] where the array elements are much smaller than the array spacing (e.g., $D = 2\lambda_0$, $d = 6\lambda_0$). The application of the fixed weights shown in the bottom row of Fig. 8b leads to a high variation of the LoS coupling between the distributions because the incoherent interference between the LoS apertures in such an array is very high. As shown in Fig. 10b, the level of LoS coupling is lower and the spectral capacity is reduced; it even reaches 0 at one point. If instead of using fixed beamforming weights, we apply the SVD optimization for each single range, we reach higher spectral capacity at the cost of highly oscillating LoS coupling levels. Moreover, the beamforming weights obtained, vary highly in range. Indeed, a standard LoS MIMO has an optimal array spacing that depends on the range and frequency, i.e., $d = \sqrt{\lambda R/N}$ [12]. This comparison shows the benefit of optimizing the equivalent aperture current distributions of an array as proposed in this paper.

[1] It is worth mentioning that the coupling in an actual antenna implementation will be impacted by effects such diffraction, reflections and array mutual coupling that are not modeled here.

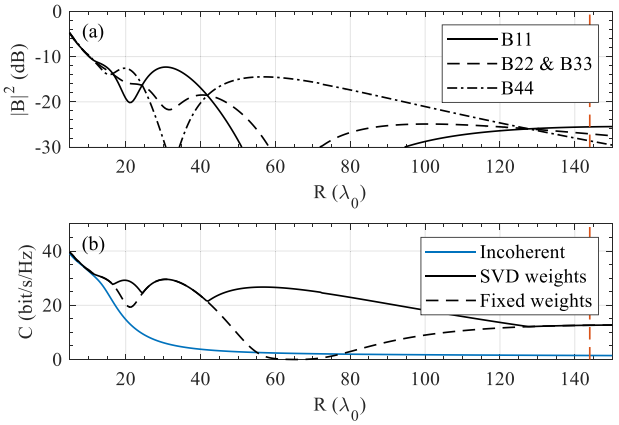


FIGURE 10. In (a) the LoS coupling between the fixed modes (B_{ij}) and in (b) the spectral capacity for the incoherent and coherent (beamforming implemented through SVD or fixed weights) array for standard LoS MIMO. In this case $D = 2\lambda_0$ and the spacing between the elements is $d = 6\lambda_0$. This corresponds to an optimal link distance of $144\lambda_0$.

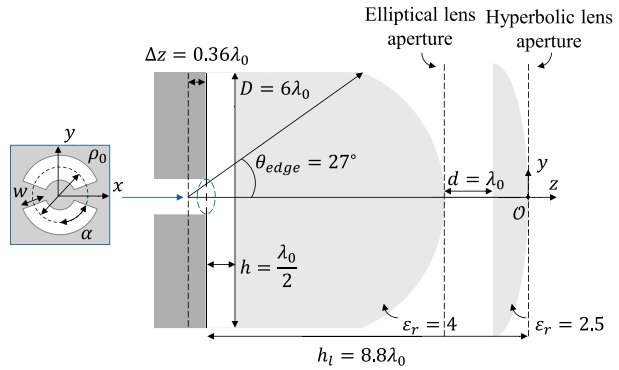


FIGURE 11. Leaky-wave lens antenna with an elliptical lens, producing a wavefront at its aperture, and a hyperbolic lens for the focusing of the phase in the radiative near-field. The double-slot feed is defined by the following parameters: $\alpha = 65.5°$, $\rho_0 = 0.52\lambda_0$, $w = 0.32\lambda_0$ and a metal thickness of $t = 0.08\lambda_0$.

VI. VALIDATION WITH FULL WAVE SIMULATIONS OF A LENS ANTENNA ARRAY

The aim of this section is to validate the LoS coupling and interference levels, presented in the previous section, using full-wave (FW) CST simulations. For this purpose, we first introduce the design of a $D = 6\lambda_0$ leaky-wave (LW) elliptical lens antenna which produces a Gaussian amplitude distribution and uniform phase at its equivalent aperture. As discussed in Section IV-C, this closely resembles the PSWF of the optimal current distribution in terms of amplitude. The required quadratic phase is achieved by a hyperbolic lens that is placed in front of the integrated lens antenna in order to focus the radiation at the desired distance F_p. The two lenses are shown schematically in Fig. 11.

A. LEAKY-WAVE LENS ANTENNA GEOMETRY

The integrated LW lens antenna consists of a waveguide feed terminated by a double-slot iris, a half-wavelength LW cavity, and the elliptical dielectric lens [21], [22]. This type of lens feed illuminates the lens surface with a nearly Gaussian beam.

The relative permittivity of the elliptical lens was chosen based on a trade-off between two properties: low permittivity LW lenses have large bandwidth [22], but high permittivity LW lenses can achieve large edge tapers [23]. We selected a permittivity of $\varepsilon_r = 4$. The double-slot iris that terminates the waveguide was designed based on [22] to achieve a wideband high return loss and to suppress the undesired TM0 leaky-wave mode which in turn improves the Gaussicity of the field radiated by the lens. The dimensions of this iris are provided in the caption of Fig. 11.

The elliptical lens geometry was optimized such that its aperture fields approximate the theoretical optimized current distribution (PSWF with $c = 3$). This was executed through a reaction integral between the equivalent aperture currents of the lens and the theoretical optimized current distribution. The equivalent aperture currents of the lens were obtained by using Geometrical Optics (GO) to propagate the primary pattern of the feed until the equivalent aperture of the elliptical lens [24]. These fields include the effect of a quarter-wavelength matching layer which reduces reflections at the lens-air interface. The field was optimized to achieve the desired edge taper by tuning the truncation angle θ_{edge} and the phase center Δz of the lens. Note that the quadratic phase distribution of the optimal current distribution was not considered in the reaction integral because the quadratic phase is produced later by the hyperbolic lens. The optimal match between the two distributions occurred for a truncation angle of $\theta_{edge} = 27°$, which is much lower than the lens critical angle of $\theta_c = 60°$, and a phase center at $z = -0.36\lambda_0$. The resulting equivalent aperture current distribution is shown in Fig. 12. The obtained currents are nearly symmetric in all planes, except at the edges of the aperture where the H-plane currents are lower than the desired -11.4 dB taper. The cross-polarization level reaches a maximum of -14.5 dB at the edges of the aperture. Our assessment is that the elliptical lens antenna reasonably resembles the desired PSWF currents in terms of both amplitude and phase.

The hyperbolic lens is placed at a distance of $1\lambda_0$ from the elliptical lens aperture as shown in Fig. 11. This lens is designed to achieve frequency-independent focusing at F_p by adding a quadratic phase. We use a low permittivity lens material $\varepsilon_r = 2.5$ to minimize reflections at the lens-air interfaces. To further minimize the impact of the lens, a quarter-wavelength matching layer is added to both sides of the lens.

Recent literature has demonstrated high-capacity communication links in the near-field using horns and slot arrays [10], [11], [25]. The horn presented in [10] has an optimized current distribution over an aperture of $9\lambda_0$, comparable to the element size presented here. However, the required horn tapering is more than $14\lambda_0$ long. The aperture size of the 2×2 slot array presented in [11] is comparable to the work presented here and is thin due to the technology. The single RLSA element with three radiating modes in [10] has a very large aperture diameter of $40\lambda_0$ and it is also very thin. By contrast, the dual-lens implementation

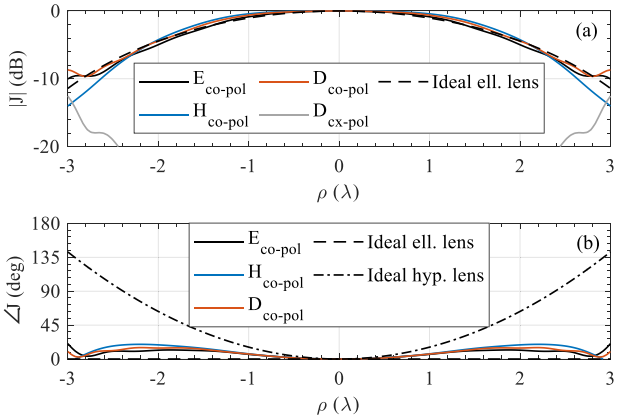


FIGURE 12. In (a) the amplitude of the GO aperture current distribution of elliptical lens in different planes of the y-component of the aperture electric current distribution are compared to the amplitude of the ideal PSWF distribution (23). In (b) the phase of the GO aperture current distribution in the different planes is compared to the ideal phase achieved by the elliptical lens and the ideal phase achieved by the hyperbolic lens.

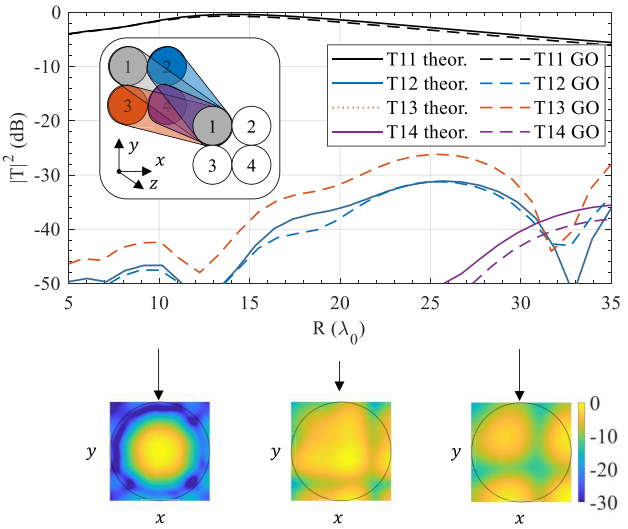


FIGURE 13. LoS coupling and individual interference levels calculated between the apertures of the optimized current distribution (solid) and the GO currents shown in Fig. 12, multiplied with an ideal quadratic phase focusing at $F_p = 11.4\lambda_0$. The interference term T_{13} is in the *E*-plane of the feed and the interference term T_{12} is in the *H*-plane of the feed as can be seen from the inset with the numbering of the lens antennas. Below, the radiated field of the four Tx apertures on Rx_1 is plotted which demonstrates the effect of the increased interference with range.

presented here is much thicker. However, this implementation is only used to validate the transfer matrix model; a prototype would have both lenses integrated into one. Furthermore, in contrast to the other implementations, lens-based solutions are suitable for millimeter and sub-millimeter wavelengths and for wide bandwidths [22], [23], and also with integrated technology [26].

B. COMPARISON GO CURRENTS TO THEORETICAL OPTIMIZED CURRENT DISTRIBUTION

The amplitude of the equivalent current distribution on the elliptical lens is only approximately equal to the amplitude of the optimized current distribution (Fig. 12). The reasons for this are the non-idealities of the lens feed and diffraction effects at the lens' edge. To study these effects, we compare the LoS coupling and individual interference levels of both current distributions. For fair comparison we multiply the lens aperture current distribution with the same quadratic phase term used for the theoretically optimized current distribution, (23) ($F_p = 11.4\lambda_0$). The coupling is again calculated as described in Appendix A. The results are shown in Fig. 13. The LoS coupling and individual interferences are generally in good agreement when using both methods. The largest mismatch is found when calculating the interference T_{13}, which is the coupling between the two lenses offset in the *E*-plane. A more symmetric feed design would lead to a better agreement.

C. CST SIMULATION RESULTS BETWEEN TWO 2X2 LENS ARRAYS

Using the previously described lens antenna as an array element, including the hyperbolic focusing lens, we validate the proposed design methodology and lens solution using FW CST simulations of the link between two arrays of 2×2 elements, as shown in Fig. 1.

In contrast to the model based on the transfer matrix using theoretically optimized current distributions, the full wave model also captures the effects of port impedance mismatch and antenna radiation efficiency, the effects of mutual coupling between the elements within an array (< -40 dB), and lens finiteness effects.

To fairly compare the transfer matrix of the GO currents with an ideal quadratic phase to the CST S-parameters, we renormalize these S-parameters to compensate for the effect of the radiation efficiency. The resulting renormalized transfer matrix obtained from the full-wave simulations is:

$$T_{ij}^{CST} = \frac{S_{ij}^{CST}}{P_{ap}} P_{in} = \frac{S_{ij}^{CST}}{\eta_{rad}}, \tag{31}$$

where P_{ap} is the power calculated at the hyperbolic antenna aperture in the case of a single lens and P_{in} is the input power of the waveguide port. The radiation efficiency of this antenna design is equal to 89% at $f = 270$ GHz.

The effect of the port impedance mismatch is also not considered in the theoretically optimized current distribution model. The resulting standing wave from this is visible in Fig. 14, where the FW radiated electric field in the channel is shown for a link distance of $R = 35\lambda_0$. The standing waves are more pronounced as the link distance decreases. Although reflections at the air-dielectric interfaces also contribute to these standing waves, their contribution has been minimized by the quarter-wavelength matching layers on the lenses. The effect of the standing waves on the S-parameters is minimized by time gating (TG) only the first LoS pulse.

The theoretically achievable spectral capacity is calculated using the various approaches: using the ideal PSWF distribution, using the GO-propagated current distribution, and using the FW CST array simulation. The results using the three

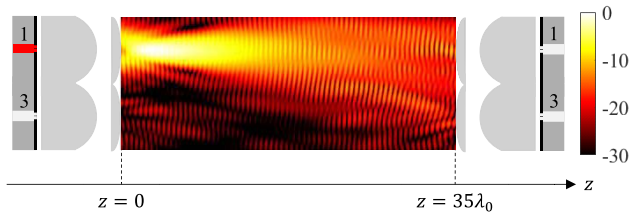


FIGURE 14. Full-wave CST results of the amplitude of radiated field from top left aperture (feed highlighted with red) in y-z-plane (E-plane), apertures 1 and 3.

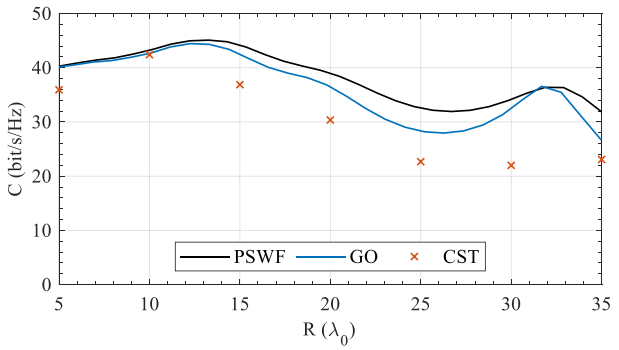


FIGURE 15. Theoretical spectral capacity from all four array elements, calculated using the results of the normalized transfer matrix model and from the TG CST results.

methods are compared in Fig. 15. The mismatch between the spectral capacity calculated for the PSWF and the GO current distribution is due to an inaccurate representation of a realistic antenna by the theoretical distribution in the E-plane as described previously. By contrast, there is a good match between the spectral capacity calculated using the GO current distribution and FW CST results.

From Fig. 15 one can also see that until $R \approx 15\lambda_0$, before which the array is noise limited, a spectral capacity of about 35 bit/s/Hz can be obtained. Within half of the far-field ($R < 35\lambda_0$), the spectral capacity levels remain above 15 bit/s/Hz, which is higher than 1 Tbps using a bandwidth of 70 GHz. Further work is required to model the impact of standing waves between the lens arrays, frequency-dependent transmit and noise power and, misalignment.

VII. CONCLUSION

A design methodology for arrays that can reach extremely high theoretical channel spectral capacity levels over half the far-field distance of the single array element is proposed. The methodology proposes an equivalent aperture current distribution that optimizes the SNIR, and therefore the spectral capacity, by means of the definition of an edge taper and focal distance requirement. This is achieved by implementing a quadratic phase distribution on the array element equivalent aperture. The solution this methodology provides is scalable with link distance, antenna geometry, number of array elements, and RF requirements thereby generating as many independent data streams as there are LoS links.

The optimal current distribution for the specific scenario described in this paper was realized using 2 × 2 lens antenna arrays with a diameter of $6\lambda_0$ at 270 GHz. Full-wave simulations validate the proposed model and design methodology when the lens feed is accurately modeled. Finally, it was substantiated that the arrays with optimized aperture current distributions have the same coupling as when using beamforming techniques – without phase control per element. It was also shown that when the equivalent aperture current distributions of the array are optimized, it is possible to use fixed beamforming weights over the incoherent region. Further work is required to model the impact of standing waves between the lens arrays, frequency-dependent transmit and noise power and misalignment. This will be the objective of future work. It is also shown that the proposed design methodology results in coupling between individual apertures similar to the coupling between orthogonal modes distributed over the entire array.

APPENDIX A
CALCULATION OF TRANSFER MATRIX USING HUYGENS' SOURCE CURRENT DISTRIBUTIONS

In this work, focusing quasi-optical (QO) antennas are modeled through an equivalent current distribution located on top of the QO antennas (see Fig. 1), as done in [6]. It is assumed that the electric and magnetic fields radiated by the QO antennas are approximated well by a Huygens' source current distribution. This means that the equivalent electric and magnetic current densities, $\vec{j}$ and $\vec{m}$, respectively, are orthogonal to each other and that their magnitude can be related through the impedance of free space ζ_0 as:

$$j = \frac{m}{\zeta_0}. \tag{32}$$

The aperture over which these current densities are modeled is defined through a function called domain$(\vec{\rho}', S_0)$ which equals 1 when $\vec{\rho}'$ lies inside S_0. We assume a normalization of the magnetic field to directly obtain the impedance values when evaluating the coupling between apertures. The normalization is the following:

$$\vec{h}(\vec{\rho}) = -\frac{I_0}{D} m(\rho)\hat{x}, \tag{33}$$

where I_0 is the current the feeding the antenna, D is the linear dimension of the antenna aperture, and where $m(\rho)$ represents a complex-valued distribution whose maximum value is normalized to one in the considered domain S_0, referring to Fig. 16. The equivalent electric and magnetic aperture currents of a transmit and receive aperture can then be defined in general as:

$$\vec{j}_{i,j}(\vec{\rho}) = -\frac{I_0}{D} g_{i,j}(\rho)\text{domain}(\vec{\rho}, S_0)\hat{y}, \tag{34}$$

$$\vec{m}_{i,j}(\vec{\rho}) = \pm\frac{\zeta_0 I_0}{D} g_{i,j}(\rho)\text{domain}(\vec{\rho}, S_0)\hat{x}. \tag{35}$$

The change in the sign of the magnetic current is to ensure radiation of the fields in the $-\hat{z}$ direction for the Rx antenna

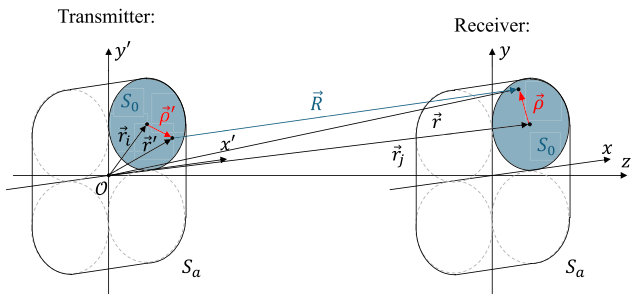


FIGURE 16. Vector definition for calculation of coupling between the apertures of two arrays that are facing each other. In the case of coupling between apertures the integration area is defined by S_0. When the coupling between beamforming modes is calculated, the area of integration is defined by S_a, including all individual apertures.

elements. It is worth noting that, locally, this approximation is consistent with GO ray field propagation.

The entries T_{ij} of the transfer matrix $\boldsymbol{T}$, discussed in Section II-A, describe the signal coupling between the Tx aperture i, Tx_i, and the Rx aperture j, Rx_j. Hence, diagonal entries T_{ii} represent the LoS coupling of the desired signal and the off-diagonal entries T_{ij} represent the interference from different channels. The individual entries are calculated using the procedure in [6] as:

$$T_{ij} = \frac{V^i_{oc} I^j_0}{\sqrt{16 P^i_{rad} P^j_{rad}}}, \tag{36}$$

where $P^{i,j}_{rad}$ represents the radiated power from both apertures which, for electrically large apertures, can be approximated by:

$$P^j_{rad} \approx \frac{\zeta_0}{2} \iint_{S_0} \left| \frac{I_0}{D} g_j(\rho) \right|^2 dA. \tag{37}$$

To calculate the numerator of (36), a reaction integral is evaluated between the electric and magnetic fields radiated by the equivalent current distributions of Tx_i and the equivalent electric and magnetic current distributions of Rx_j, evaluated on the receiving aperture as:

$$V^i_{oc} I^j_0 = \iint_{S_0} \left[\vec{h}_i(\vec{r}) \cdot \vec{m}_j(\vec{\rho}) - \vec{e}_i(\vec{r}) \cdot \vec{j}_j(\vec{\rho}) \right] dA, \tag{38}$$

where Tx_i is defined by $\vec{\rho}\,' = \vec{r}\,' - \vec{r}_i$ and Rx_j is defined by $\vec{\rho} = \vec{r} - \vec{r}_j$ (Fig. 16). This reaction integral is maximal when the radiated fields of Tx_i are the complex conjugate of the equivalent current distribution on Rx_j. The electric and magnetic fields radiated by the equivalent electric and magnetic current distributions of Tx_i are calculated at the corresponding receiver's equivalent aperture using the RGF as:

$$\vec{e}_i(\vec{r}) = jk_0\zeta_0 \iint_{S_0} \left(\tilde{I} - \hat{R}\hat{R} \right) \vec{j}_i(\vec{\rho}\,') \frac{e^{-jk_0 R}}{4\pi R} dA - jk_0 \iint_{S_0} \left(\hat{R} \times \tilde{I} \right) \vec{m}_i(\vec{\rho}\,') \frac{e^{-jk_0 R}}{4\pi R} dA, \tag{39}$$

$$\vec{h}_i(\vec{r}) = \frac{jk_0}{\zeta_0} \iint_{S_0} \left(\tilde{I} - \hat{R}\hat{R} \right) \vec{m}_i(\vec{\rho}\,') \frac{e^{-jk_0 R}}{4\pi R} dA + jk_0 \iint_{S_0} \left(\hat{R} \times \tilde{I} \right) \vec{j}_i(\vec{\rho}\,') \frac{e^{-jk_0 R}}{4\pi R} dA, \tag{40}$$

where $\tilde{I}$ is the identity matrix and $\vec{R}$ is the vector between any points of the transmitter aperture and receiver equivalent apertures (see Fig. 16).

APPENDIX B
PROLATE SPHEROIDAL WAVE FUNCTION

For decades mathematicians, physicists, and engineers have relied on various orthogonal expansions such as Fourier, Legendre, and Chebyschev to solve a variety of problems. In this appendix, we summarize the orthogonal properties of prolate spheroidal wave functions (PSWF) and its derivation from [27]. PSWFs arose from the study of the wave equation in general ellipsoidal coordinates. When the wave equation is separated in prolate spheroidal coordinates, the resulting second-order ordinary differential equations are satisfied by the PSWFs [28]. To construct them, numerous expansions have been constructed using Legendre polynomials, spherical Bessel functions, power series.

In the following two subsections we provide the PSWF properties and possible derivation as described in [27]. These functions can be nowadays be found tabulated in mathematical software such as MATLAB [29], [30]. The last section describes the used MATLAB routine in this work.

A. PROPERTIES

The PSWFs, $\psi_n(C, t)$, are a set of bandlimited functions. They are dependent on a total of four parameters: the continuous time parameter t, the function order n, the interval on which the function is known t_0, and the bandwidth parameter C. The bandwidth parameter is given by:

$$C = t_0 \Omega, \tag{41}$$

where Ω is the finite bandwidth or cutoff frequency of $\psi_n(C, t)$ of a given order n. The PSWFs $\psi_n(C, t)$ concentrated in the interval of $[-t_0, t_0]$ are normalized eigenfunctions of the system:

$$\psi_n(C, x)\lambda_n(C) = \int_{-t_0}^{t_0} \psi_n(C, t) \frac{\sin \Omega(x - t)}{\pi(x - t)} dt, \tag{42}$$

where $\lambda_n(C)$ is the eigenvalue of the sinc kernel and can be also regarded as the index of concentration on the interval $[-t_0, t_0]$.

The eigenfunctions $\psi_n(C, t)$ are invariant to a finite Fourier transform:

$$\int_{-t_0}^{t_0} \psi_n(C, t) e^{j\omega t} = j^n \sqrt{\frac{2\pi \lambda_n(C) t_0}{\Omega}} \psi_n\left(C, \frac{\omega t_0}{\Omega}\right). \tag{43}$$

The infinite Fourier transform of $\psi_n(C,t)$ is also invariant.

$$\int_{-\infty}^{\infty} \psi_n(C,t)e^{j\omega t} = j^n\sqrt{\frac{2\pi t_0}{\Omega}}\psi_n\left(C, \frac{\omega t_0}{\Omega}\right) \tag{44}$$

This shows that $\psi_n(C,t)$ are doubly invariant to the Fourier transform. This invariance for both the finite and infinite domain states that $\psi_n(C,t)$ is bandlimited.

Another key set of properties states that $\psi_n(C,t)$ also obey a duality of orthogonality where the eigenfunctions of the previous equation are orthogonal over a finite and infinite domain. These functions are also normalized so that the following inner products obey the following:

$$\int_{-t_0}^{t_0} \psi_n(C,t)\psi_m(C,t)dt = \begin{cases} \lambda_n(C) & \text{for } n=m, \\ 0 & \text{for } n\neq m, \end{cases} \tag{45}$$

$$\int_{-\infty}^{\infty} \psi_n(C,t)\psi_m(C,t)dt = \begin{cases} 1 & \text{for } n=m, \\ 0 & \text{for } n\neq m. \end{cases} \tag{46}$$

B. DERIVATION

The simplest approach to derive the PSFWs is using the following expansion:

$$\psi_n(C,t) = \sum_{k=0}^{\infty} \beta_k^n P_k(t), \tag{47}$$

where $P_k(t)$ is the Legendre polynomials of order k. The coefficients β_k^n can be calculated from the following recurrence relation:

$$\begin{aligned} &\frac{(k+2)(k+1)}{(2k+3)\sqrt{(2k+5)(2k+1)}}C^2\beta_{k+2}^n \\ &\quad+\left(k(k+1)+\frac{2k(k+1)-1}{(2k+3)(2k-1)}C^2-\chi_j\right)\beta_k^n \\ &\quad+\frac{k(k-1)}{(2k-1)\sqrt{(2k-3)(2k+1)}}C^2\beta_{k-2}^n = 0, \end{aligned} \tag{48}$$

where χ_j are the eigenvalues. To find the eigenvalue $\lambda_n(C)$, we can use the radial solution in spheroidal wave coordinates of the Helmholtz wave equation of the first kind, $R_{0n}^{(1)}(C,1)$:

$$\lambda_n(C) = \frac{2C}{\pi}\left[R_{0n}^{(1)}(C,1)\right]^2, \quad n=0,1,2,\ldots \tag{49}$$

For the evaluation of $\psi_n(C,t)$, we can use the angular solution of the Helmholtz wave equation of the first kind:

$$\psi_n(C,t) = \frac{\sqrt{\lambda_n(C)/t_0}}{\mu_n(C)}S_{0n}\left(C, \frac{t}{t_0}\right), \tag{50}$$

where,

$$\mu_n(C) = \sqrt{\int_{-1}^{1}(S_{0n}(C,t))^2dt}. \tag{51}$$

The eigenfunctions $\psi_n(C,t)$ are simply normalized versions of the spheroidal wave functions of order zero. To find the solution $S_{0n}(C,t)$, we apply the following expansion:

$$S_{mn}(C,t) = \sum_{r=0,1}^{\infty} d_r^{mn}(C)P_{m+r}^m(t), \tag{52}$$

where $P_{m+r}^m(t)$ is the Legendre polynomial while $d_r^{mn}(C)$ represents the expansion coefficient.

C. MATLAB ROUTINE

The MATLAB DPSS function implements a discretized PSWF function that solves (42) with a different normalization [31]:

$$\psi_n(c,x)\lambda_n(c) = \int_{-1}^{1}\psi_n(c,y)\frac{\sin c(x-y)}{\pi(x-y)}dy. \tag{53}$$

This equation corresponds to (19) and (20) from [7] where c is equal to (20) in this work.

APPENDIX C
DERIVATION OF COUPLING BETWEEN BEAMFORMING CURRENT DISTRIBUTIONS

To calculate the beamforming transfer matrix $\boldsymbol{B}$ with beamforming weights as described in (27) we start by defining the current distribution over the entire array. Referring to Fig. 16, the current distribution over the entire transmit and receive arrays are defined as the summation of the currents of the individual apertures in their corresponding position, with $\vec{\rho}\,' = \vec{r}\,' - \vec{r}_i$ and $\vec{\rho} = \vec{r} - \vec{r}_j$, (34) and (35), multiplied by their corresponding weights as:

$$\vec{j}_m(\vec{r}\,') = \sum_{i=1}^{M} w_{m,i}\vec{j}_i(\vec{\rho}\,'); \quad \vec{j}_n(\vec{r}) = \sum_{j=1}^{M} w_{n,j}^*\vec{j}_j(\vec{\rho}), \tag{54}$$

$$\vec{m}_m(\vec{r}\,') = \sum_{i=1}^{M} w_{m,i}\vec{m}_i(\vec{\rho}\,');$$

$$\vec{m}_n(\vec{r}) = \sum_{j=1}^{M} w_{n,j}^*\vec{m}_j(\vec{\rho}). \tag{55}$$

Let us define the radiated electric and magnetic fields corresponding to a specific distribution at the location of the receiver array equivalent aperture. These can be written as:

$$\begin{aligned} \vec{e}_m(\vec{r}) &= jk_0\zeta_0\iint_{S_a}\left(\tilde{I}-\hat{R}\hat{R}\right)\sum_{i=1}^{M} w_{m,i}\vec{j}_i(\vec{\rho}\,')\frac{e^{-jk_0R}}{4\pi R}dA \\ &\quad - jk_0\iint_{S_a}\left(\hat{R}\times\tilde{I}\right)\sum_{i=1}^{M} w_{m,i}\vec{m}_i(\vec{\rho}\,')\frac{e^{-jk_0R}}{4\pi R}dA \end{aligned} \tag{56}$$

$$\vec{h}_m(\vec{r}) = \frac{jk_0}{\zeta_0}\iint_{S_a}\left(\tilde{I}-\hat{R}\hat{R}\right)\sum_{i=1}^{M} w_{m,i}\vec{m}_i(\vec{\rho}\,')\frac{e^{-jk_0R}}{4\pi R}dA + jk_0\iint_{S_a}\left(\hat{R}\times\tilde{I}\right)\sum_{i=1}^{M} w_{m,i}\vec{j}_i(\vec{\rho}\,')\frac{e^{-jk_0R}}{4\pi R}dA, \quad (57)$$

where the fields are now evaluated over the equivalent aperture of the entire transmitter array S_a. As the transmit weights are constants and identical for the electric and magnetic currents, they can be taken out of the integral, allowing us to rewrite the expression for the modal fields as the superposition of the fields radiated by each aperture with the appropriate weight. The reaction integral between the radiated modal fields and the model currents can now be evaluated over the receive array S_a similar to (38). When using the expressions of the modal currents and modal fields, the reaction integral is simplified to:

$$V_{oc}^m I_0^n = \sum_{i=1}^{M} w_{m,i}\left(\sum_{j=1}^{M} w_{n,j}^*\iint_{S_0}\left[\vec{h}_i(\vec{r})\cdot\vec{m}_j(\vec{\rho}) - \vec{e}_i(\vec{r})\cdot\vec{j}_j(\vec{\rho})\right]dA\right) = \sum_{i=1}^{M} w_{m,i}\sum_{j=1}^{M} w_{n,j}^* V_{oc}^i I_0^j. \quad (58)$$

This is also the superposition of the reaction integral of the fields and currents of the individual apertures (38) multiplied with the corresponding transmitter and receiver weights, evaluated over the entire Rx array equivalent aperture. The power radiated per distribution by the array must be calculated from the current over the array equivalent aperture, which can be done as:

$$P_{rad}^m = \frac{\zeta_0}{2}\iint_{S_a}|\vec{j}_m(\vec{r}\,')|^2 dA \approx \sum_{i=1}^{M}|w_{m,i}|^2 P_{rad}^i. \quad (59)$$

This expression can be simplified to the superposition of the radiated power of a single aperture (37) with the corresponding weights of the distribution. This simplification can be made by recognizing that, due to the physical separation of the current distributions in the array, the integrals of the individual apertures within the array aperture are all equal to the integral of a single aperture over the area of a single aperture at the origin. The coupling between beamforming distributions m and n can now be written as:

$$b_{mn} = \frac{V_{oc}^m I_0^n}{\sqrt{16 P_{rad}^m P_{rad}^n}} = \frac{\sum_{i=1}^{M} w_{m,i}\sum_{j=1}^{M} w_{n,j}^* V_{oc}^i I_0^j}{\sqrt{16\sum_{i=1}^{M}|w_{m,i}|^2 P_{rad}^i \sum_{j=1}^{M}|w_{n,j}^*|^2 P_{rad}^j}}. \quad (60)$$

This means that the *beamforming* coupling can be calculated by multiplying the *individual aperture* couplings with the corresponding weights of distributions m and n. This matrix can be calculated by multiplying the individual aperture couplings by the corresponding weights of distributions m and n. From the summations in this expression, we can recognize a part of this as the coupling matrix for the individual apertures as follows:

$$b_{mn} = \frac{\mathbf{W}_{Rx}\mathbf{T}\mathbf{W}_{Tx}^T}{\sqrt{\sum_{j=1}^{M}|w_{n,j}^*|^2\sum_{i=1}^{M}|w_{m,i}|^2}}, \quad (61)$$

where the matrices containing the weights are those defined in (27).

REFERENCES

[1] T. S. Raspatory et al., "Wireless communications and applications above 100 GHz: Opportunities and challenges for 6G and beyond," *IEEE Access*, vol. 7, pp. 78729–78757, 2019.

[2] H. Tataria, M. Shafi, M. Dohler, and S. Sun, "Six critical challenges for 6G wireless systems: A summary and some solutions," *IEEE Veh. Technol. Mag.*, vol. 17, no. 1, pp. 16–26, Mar. 2022.

[3] H. Zhang, N. Shlezinger, F. Guidi, D. Dardari, and Y. C. Eldar, "6G wireless communications: From far-field beam steering to near-field beam focusing," *IEEE Commun. Mag.*, vol. 61, no. 4, pp. 72–77, Apr. 2023.

[4] *IEEE Standard for High Data Rate Wireless Multi-Media Networks–Amendment 2: 100 Gb/s Wireless Switched Point-to-Point Physical Layer*, IEEE Standard 802.15.3d-2017 (Amendment to IEEE Std 802.15.3-2016 as amended by IEEE Std 802.15.3e-2017), 2017.

[5] H. Do, S. Cho, J. Park, H.-J. Song, N. Lee, and A. Lozano, "Terahertz line-of-sight MIMO communication: Theory and practical challenges," *IEEE Commun. Mag.*, vol. 59, no. 3, pp. 104–109, Mar. 2021.

[6] N. Llombart and S. O. Dabironezare, "Feasibility study of quasi-optical MIMO antennas for radiative near-field links," *IEEE Trans. Antennas Propag.*, vol. 70, no. 8, pp. 7073–7083, Aug. 2022.

[7] G. Borgiotti, "Maximum power transfer between two planar apertures in the fresnel zone," *IEEE Trans. Antennas Propag.*, vol. 14, no. 2, pp. 158–163, Mar. 1966.

[8] F. Alsolamy, W. A. Alomar, and A. Grbic, "Cylindrical vector beams for wireless power transfer," *IEEE Trans. Antennas Propag.*, vol. 69, no. 3, pp. 1716–1727, Mar. 2021.

[9] S. Paković, S. Zhou, D. González-Ovejero, S. C. Pavone, A. Grbic, and M. Ettorre, "Bessel–Gauss beam launchers for wireless power transfer," *IEEE Open J. Antennas Propag.*, vol. 2, pp. 654–663, 2021.

[10] X. Xu, A. Mazzinghi, A. Freni, and J. Hirokawa, "Simultaneous generation of three OAM modes by using a RLSA fed by a waveguide circuit for 60 GHz-band radiative near-field region OAM multiplexing," *IEEE Trans. Antennas Propag.*, vol. 69, no. 3, pp. 1249–1259, Mar. 2021.

[11] K. Tekkouk, J. Hirokawa, and M. Ando, "Multiplexing antenna system in the non-far region exploiting two-dimensional beam mode orthogonality in the rectangular coordinate system," *IEEE Trans. Antennas Propag.*, vol. 66, no. 3, pp. 1507–1515, Mar. 2018.

[12] L. Liu et al., "Characterization of line-of-sight MIMO channel for fixed wireless communications," *IEEE Antennas Wireless Propag. Lett.*, vol. 6, pp. 36–39, 2007.

[13] C. Shannon, "Communication in the presence of noise," *Proc. IRE*, vol. 37, no. 1, pp. 10–21, Jan. 1949.

[14] W. Geyi, "The method of maximum power transmission efficiency for the design of antenna arrays," *IEEE Open J. Antennas Propag.*, vol. 2, pp. 412–430, 2021.

[15] W. Geyi, *Foundations of Applied Electrodynamics*. Hoboken, NJ, USA: Wiley, Apr. 2010.

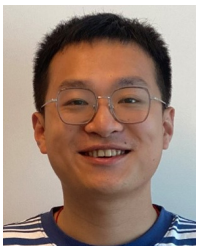
[16] T. Soejima, "Fresnel gain of aperture aerials," *Proc. Inst. Electr. Eng.*, vol. 110, no. 6, pp. 1021–1027, 1963.

[17] S. Takeshita, "Power transfer efficiency between focused circular antennas with Gaussian illumination in fresnel region," *IEEE Trans. Antennas Propag.*, vol. 16, no. 3, pp. 305–309, May 1968.

[18] N. Llombart, B. Blázquez, A. Freni, and A. Neto, "Fourier optics for the analysis of distributed absorbers under THz focusing systems," *IEEE Trans. THz Sci. Technol.*, vol. 5, no. 4, pp. 573–583, Jul. 2015.
[19] D. Slepian, "Prolate spheroidal wave functions, fourier analysis and uncertainty—IV: Extensions to many dimensions; generalized prolate spheroidal functions," *Bell Syst. Techn. J.*, vol. 43, no. 6, pp. 3009–3057, Nov. 1964.
[20] E. Telatar, "Capacity of multi-antenna Gaussian channels," *Eur. Trans. Telecommun.*, vol. 10, no. 6, pp. 585–595, 1999.
[21] *Breaking the 100 Gbps Barrier—Extract From the Ericsson Microwave Outlook Report*, Ericsson, Stockholm, Sweden, 2019.
[22] M. Arias Campo, D. Blanco, S. Bruni, A. Neto, and N. Llombart, "On the use of fly's eye lenses with leaky-wave feeds for Wideband communications," *IEEE Trans. Antennas Propag.*, vol. 68, no. 4, pp. 2480–2493, Apr. 2020.
[23] N. Llombart, G. Chattopadhyay, A. Skalare, and I. Mehdi, "Novel terahertz antenna based on a silicon lens fed by a leaky wave enhanced waveguide," *IEEE Trans. Antennas Propag.*, vol. 59, no. 6, pp. 2160–2168, Jun. 2011.
[24] H. Zhang, S. O. Dabironezare, G. Carluccio, A. Neto, and N. Llombart, "A fourier optics tool to derive the plane wave spectrum of quasi-optical systems [EM programmer's notebook]," *IEEE Antennas Propag. Mag.*, vol. 63, no. 1, pp. 103–116, Feb. 2021.
[25] M. Ettorre and D. G. Ovejero, "High speed and resilient wireless interconnects in the near field," in *Proc. Int. Workshop Antenna Technol. (iWAT)*, 2023, pp. 1–4.
[26] H. Zhang, S. Bosma, A. Neto, and N. Llombart, "A dual-polarized 27 dBi scanning lens phased array antenna for 5G point-to-point communications," *IEEE Trans. Antennas Propag.*, vol. 69, no. 9, pp. 5640–5652, Sep. 2021.
[27] I. C. Moore and M. Cada, "Prolate spheroidal wave functions, an introduction to the Slepian series and its properties," *Appl. Comput. Harmon. Anal.*, vol. 16, no. 3, pp. 208–230, 2004.
[28] D. Slepian and H. O. Pollak, "Prolate spheroidal wave functions, fourier analysis and uncertainty—I," *Bell Syst. Techn. J.*, vol. 40, no. 1, pp. 43–63, 1961.
[29] C. Flammer, *Spheroidal Wave Functions*. Redwood City, CA, USA: Stanford Univ., 1957.
[30] J. A. Stratton, P. M. Morse, L. J. Chu, J. D. C. Little, and F. J. Corbato, *Spheroidal Wave Functions*. Cambridge, MA, USA: MIT press, 1959.
[31] D. B. Percival and A. T. Walden, *Spectral Analysis for Physical Applications*. Cambridge, U.K.: Cambridge Univ., 1993.



N. BESCHOOR PLUG (Graduate Student Member, IEEE) received the M.Sc. degree in electrical engineering from the Delft University of Technology, Delft, The Netherlands, in 2021, where she is currently pursuing the Ph.D. degree with Terahertz Sensing Group. Her Ph.D. focuses on near-field communication system using lens arrays. During her master's, she worked on superconducting circuits for THz astronomy and worked part-time as a Junior Innovator with TNO Defense, Security and Safety, The Hague, The Netherlands. Her research interests include the LoS MIMO systems, near-field communication, and quasi-optical systems.



J. TAN received the M.Sc. degree in electrical engineering from the Delft University of Technology, Delft, The Netherlands, in 2023.



S. BOSMA (Member, IEEE) received the M.Sc. and Ph.D. degrees (cum laude) in electrical engineering from the Delft University of Technology, Delft, The Netherlands, in 2017 and 2023, respectively.

His Ph.D. project focused on scanning lens phased array antennas at submillimeter wavelengths. This project was in collaboration with NASA's Jet Propulsion Laboratory, Pasadena, CA, USA, where he spent five months in the Submillimeter-Wave Advanced Technology Group as a Visiting Student Researcher from 2018 to 2019. His Ph.D. research has led to more than 30 journal and conference contributions and four best-paper nominations. He is currently a Senior RF/mmWave Circuit Engineer with NXP Semiconductors, Eindhoven, The Netherlands, working on the next generation of automotive radars.



G. CARLUCCIO (Senior Member, IEEE) was born in 1979 and grew up in Ortelle, Italy. He received the Laurea degree in telecommunications engineering and the Ph.D. degree in information engineering from the University of Siena, Siena, Italy, in 2006 and 2010, respectively.

From 2008 to 2009 he was an Invited Visiting Scholar with the ElectroScience Laboratory, Department of Electrical and Computer Engineering, The Ohio State University, Columbus, OH, USA. From 2010 to 2014, he was a Researcher with the Department of Information Engineering and Mathematics, University of Siena. From 2012 to 2013, he was a Researcher with the Department of Electronics and Telecommunication, University of Florence, Florence, Italy. From 2012 to 2013, he was a Visiting Researcher with the Department of Microelectronics, Delft University of Technology, Delft, The Netherlands, where he also a Researcher from 2014 to 2018. Since 2018, he has been a RF Circuits and Antenna Scientist with NXP Semiconductors, Eindhoven, The Netherlands, where he focuses on RF devices for automotive radar applications. His research interests deal with electromagnetic wave theory, mainly focused on asymptotic high-frequency techniques for electromagnetic scattering and propagation; and with modeling and design of antennas, quasi-optical systems, and periodic structures: mainly, reflector antennas, dielectric lens antennas, reflectarrays, connected arrays, THz antennas based on photoconductive materials, and antennas-in-package.

Dr. Carluccio was the recipient of the 2018 EurAAP International "Leopold B. Felsen Award for Excellence in Electrodynamics", and of the 2010 URSI Commission B Young Scientist Award at the International Symposium on Electromagnetic Theory, where he also received the third prize for the Young Scientist Best Paper Award.



A. NETO (Fellow, IEEE) received the Laurea degree (summa cum laude) in electronic engineering from the University of Florence, Florence, Italy, in 1994, and the Ph.D. degree in electromagnetics from the University of Siena, Siena, Italy, in 2000.

Part of his Ph.D. degree was developed at the European Space Agency Research and Technology Center, Noordwijk, The Netherlands. He was with the Antenna Section, European Space Agency Research and Technology Center, for more than two years. From 2000 to 2001, he was a Postdoctoral Researcher with the California Institute of Technology, Pasadena, CA, USA, where he was with the Submillimeter Wave Advanced Technology Group. From 2002 to 2010, he was a Senior Antenna Scientist with TNO Defense, Security, and Safety, The Hague, The Netherlands. In 2010, he was appointed as a Full Professor of applied electromagnetism with the Department of Electrical Engineering, Mathematics and Computer Science, Delft University of Technology, The Netherlands, where he formed and leads the THz Sensing Group. His research interests include the analysis and design of antennas, as well as time domain sensing and radiometry.

Dr. Neto was a recipient of the European Research Council Starting Grant to perform research on advanced antenna architectures for THz sensing systems in 2011, the H. A. Wheeler Award for the best applications paper of 2008 in the IEEE Transactions on Antennas and Propagation and multiple times of the Best Paper Prizes of the European Conference on Antennas and Propagation. He was an Associate Editor of the IEEE TRANSACTIONS ON ANTENNAS AND PROPAGATION, IEEE ANTENNAS AND WIRELESS PROPAGATION LETTERS, and currently of the IEEE TRANSACTIONS OF THZ SCIENCE AND TECHNOLOGY. He is a Member of the Technical Board of the European School of Antennas and an organizer of the course on THz antenna imaging techniques.



N. LLOMBART (Fellow, IEEE) received the master's degree in electrical engineering and the Ph.D. degree in electromagnetics from the Polytechnic University of Valencia, Valencia, Spain, in 2002 and 2006, respectively.

During her master's degree studies, she spent one year with the Friedrich Alexander University of Erlangen Nuremberg, Erlangen, Germany, and worked with the Fraunhofer Institute for Integrated Circuits, Erlangen, Germany. From 2002 to 2007, she was with the Antenna Group, TNO Defense, Security and Safety Institute, The Hague, The Netherlands, working as a Ph.D. student and afterward as a Researcher. From 2007 to 2010, she was a Postdoctoral Fellow with the SubmillimeterWave Advance Technology Group, Jet Propulsion Laboratory, California Institute of Technology, Pasadena, CA, USA. She was a "Ramón y Cajal" Fellow with the Optics Department, Complutense University of Madrid, Madrid, Spain, from 2010 to 2012. In 2012, she was with the THz Sensing Group, Technical University of Delft, Delft, The Netherlands, where she has been a Full Professor since 2018. She has coauthored more than 200 journal and international conference contributions in the areas of antennas and terahertz systems.

Dr. Llombart was the corecipient of the H. A. Wheeler Award for the Best Applications Paper of 2008 in IEEE TRANSACTIONS ON ANTENNAS AND PROPAGATION, the 2014 THz Science and Technology Best Paper Award of the IEEE Microwave Theory and Techniques Society, and several NASA awards. She was also the recipient of the 2014 IEEE Antenna and Propagation Society Lot Shafai Mid-Career Distinguished Achievement Award. In 2015, she was the recipient of European Research Council Starting Grant. She is a Board Member of the International Society of Infrared, Millimeter, and Terahertz Waves and, since 2023, an Editor in Chief of the IEEE TRANSACTIONS ON TERAHERTZ SCIENCE AND TECHNOLOGY. In 2019, she was appointment IEEE Fellow for contributions to millimeter and submillimeter wave quasi-optical antennas.